A contact mechanics study of 3D frictional conformal contact

Julio Blanco-Lorenzo, Javier Santamaria [*], Ernesto G. Vadillo, Nekane Correa

Department of Mechanical Engineering, University of the Basque Country UPV/EHU, Plaza Ingeniero Torres Quevedo 1, 48013 Bilbao, Spain

ABSTRACT

A contact mechanics study of three-dimensional conformal contact with friction is presented, based on numerical calculations with Finite Element models and an extension of Kalker's exact contact theory which takes into account the effects of conformity. Both the normal and the tangential parts of the contact problem are studied in situations with different conformity levels, up to total contact angle variations in the contact patch of about 100°, assessing the particular characteristics brought about by conformity and the differences with respect to non-conformal contact. The study may be of interest in important industrial applications where conformal contact may be found, such as rolling bearings or the wheel-rail case.

1. Introduction

It is essential to use adequate contact models in vehicle dynamic MBS simulations. Precise contact modelling is even more imperative for the study of tribological phenomena in the contact interface such as wear and rolling contact fatigue. Notably in the wheel-rail case, the hypothesis of non-conformity is adopted as a simplifying assumption in most wheel-rail rolling contact theories. However, in some situations the contact area may become considerably curved in the lateral direction, thereby compromising the adequacy of a non-conformal analysis. Moreover, conformal rolling contact is also common in other industrial application as important as rolling bearings.

2D conformal cylindrical contact is characteristic of pinned joints, which are present in numerous engineering applications, and has been extensively studied in the literature. Following the work of Persson [1], in Ref. [2] the formulation of the 2D conformal cylindrical contact without friction was developed, obtaining the load-contact angle variation relationship in closed form, and extending the range of validity of the formulation to any value of Dundurs' first material parameter. In Ref. [3] the study was extended for the case of non-zero Dundurs' second material parameter, solving numerically the governing integral equations of the problem. Further, an analytical approximation was proposed for the load-contact angle variation relationship, based on the assumption, verified by the numerical calculations in the work, that the impact of Dundurs' second material parameter on the pressure distribution (for a given contact angle variation) can be neglected. The analytical load-contact angle variation relationship was also derived in Ref. [4] for the case of identical materials in contact, and a fracture mechanics study

was conducted considering a radial crack emanating from the surface of the circular hole of the plate. In Refs. [5,6] the formulation for the 2D conformal cylindrical contact problem with friction was developed, for the case of rigid and elastic pin respectively. The influence of remote stresses in the plate was incorporated in the analysis. The analytical Green's functions of the displacements of the pin and the hole subject to boundary point loadings were used, and a numerical method was proposed to solve the governing singular integral equations of the problem, valid provided the contact is not split in more than one contact patch. Double conforming cylindrical contacts without friction, in which an intermediate annular elastic body between the pin and the infinite elastic plate with a hole was present, were studied in Refs. [7,8]. The displacements of the pin and the plate were calculated making use of their corresponding Green's functions, and those of the ring were calculated by means of a Fourier series technique. In Ref. [8] the model was extended to cope with interference in the contact, and the influence of geometric irregularities on the resulting contact pressure distributions was studied. Other references of studies about 2D conformal contact may be found in Ref. [9] for instance.

The works about 3D conformal contact in the literature are comparatively few compared with 2D contact. Refs. [10,11] are early examples of wheel-rail conformal frictionless contact studies. The study of frictional contact entails more complexity, and has been less studied than frictionless contact. In Ref. [12] an analysis method for conformal contact problems including friction in the interface was proposed. The normal part of the contact problem was solved with a simplified procedure assuming an elastic behaviour of the solids in contact similar to the elastic half-space, and the tangential part of the contact problem was

solved with FASTSIM [13,14], but accounting for the non-flat geometry in the calculation of the rigid slip velocities. A simplified method based on the strip theory was used in Chapter 8.5 of [15] to study frictional conformal rolling contact. STRIPES [16,17] is another simplified frictional rolling contact algorithm, which is based on the idea of dividing the contact patch in longitudinal strips, and is able to deal with contact cases with conformal geometries. In Ref. [18] Kalker's exact rolling contact theory [13,14] was generalized for conformal contact by replacing the half-space influence coefficients (ICs) by appropriate ICs for non-planar geometries, and was later used in Ref. [19] for a case study with conformal contact. The same approach was applied in Ref. [20] with Kalker's exact contact theory programmed in the CONTACT software [21].

Recently, the authors have investigated about the three-dimensional wheel-rail conformal rolling contact [22,23], considering cases with moderate total contact angle variations in the contact area, of up to about 41° in the lateral direction. In the present work the study on three-dimensional conformal contact with friction is further extended to higher levels of conformity. For this purpose, both FE models and an extension of the exact contact theory for conformal contact, previously described by the authors in Ref. [23] and which will be referred to as CECT (Conformal Exact Contact Theory) here, are used. The qualitative differences between conformal and non-conformal contact are pointed out, and the adequacy of currently widely used non-conformal contact models under different conformal contact situations is discussed. In this way, the paper provides insight into some phenomena related to 3D conformal contact, and examines the errors which may arise when disregarding the effects of conformity in the analysis. The work may be of particular interest in applications in which accurate contact mechanics results are necessary in conformal contact conditions, such as in analyses of damage phenomena in the contact interface like wear.

2. Description of the models

In this section the most relevant aspects of the models used in this work are summarized. On the one hand, Finite Element models, and on the other hand, an extension of Kalker's exact rolling contact theory for conformal contact, developed along the same lines as in Refs. [18] and [20] and designated here as CECT, are used. A more detailed description of the models may be found in Ref. [23].

Before going further, a brief description of the representation of the conformal contact geometry is given. The three-dimensional contact between a body of revolution and a body with constant cross section in the longitudinal direction is considered, which will be called the wheel and the rail respectively. The contact is assumed to be conformal in the plane perpendicular to the rolling direction only, as represented in Fig. 1, and non-conformal in the longitudinal or rolling direction. As the contact angle is variable in the lateral direction, in order to provide a quick measure of it in each studied case, the concept of the mean contact angle is used. This is defined as the contact angle at the first or rigid point of contact (which will usually be at or near the central point of the contact patch). The local quantities of interest in the contact (stresses, deformations, etc.) are expressed in the local contact coordinate system. This is a Cartesian coordinate system tangent to each point in the contact, its three principal orthogonal directions being defined as the longitudinal (rolling) x, the tangential lateral s, and the normal n axes. The origin of the x and s coordinates is taken to be at the first or rigid point of contact.

2.1. Finite Element models

The Finite Element Method offers the possibility to model diverse physical phenomena, considering dynamic effects, complex material behaviours or contact interactions for example. However, its application to rolling contact mechanics poses some challenges, coming basically from the fact that the region to be modelled has to be typically much larger than the (contact) region of interest. The resulting models frequently have hundreds of thousands of degrees of freedom, and have high computational costs. Additionally, usually a fine-tuning process of the model and associated parameters such as numerical tolerances or incrementation controls becomes necessary in order to obtain valid results for a given application, see Ref. [24] for example.

In this work detailed 3D Finite Element models are constructed meshing a part of both solids in contact with linear solid elements, with a high refinement around the contact area so that the contact patch is discretized in up to around 40 elements in each direction. With these models, static contact, transient or steady rolling contact cases can be simulated. The contact simulations are performed imposing predefined motions to the central point of the wheel in successive steps. For the steady state rolling contact simulations (Section 3.3) the results are obtained after a rolling length of about 3 times the total longitudinal
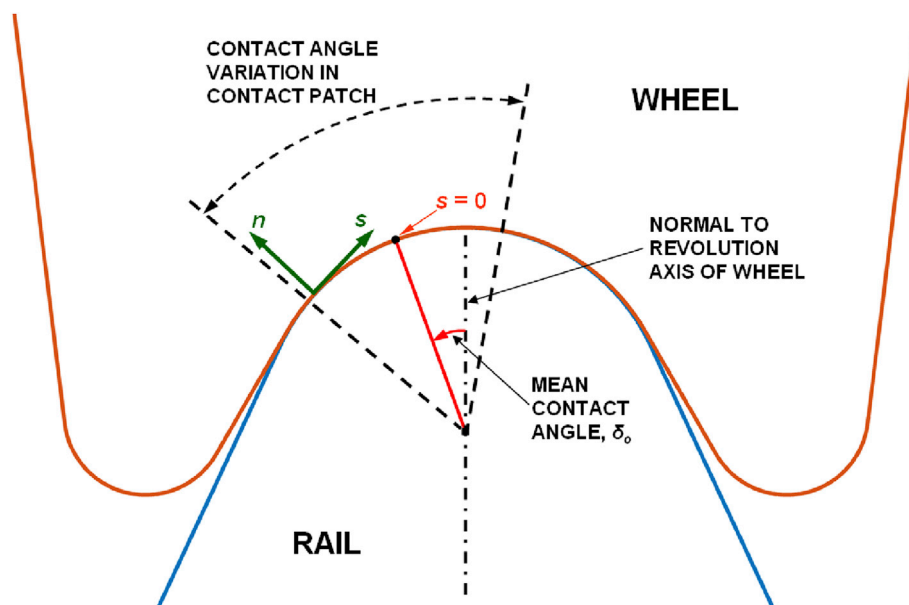

Fig. 1. Conformal contact geometry with definition of mean contact angle δ_o and local contact coordinate system with directions s and n. Section view, perpendicular to the rolling direction x.

dimension of the contact patch, executed in about 100 substeps. It is verified that in the cases shown in this work the subsequent variation of the results after this point is small (i.e. the results have almost converged to the steady state rolling contact situation).

2.2. Conformal Exact Contact Theory

Kalker's exact contact theory is applicable to general non-Hertzian contact geometries, to contact with elastically similar or dissimilar materials, and to non-stationary or to stationary rolling contact problems in elastostatics. Few simplifications of the mechanical behaviour of the contacting bodies are done; these are limited to linearity, absence of inertia forces and, in its usual form, the half-space assumption. In its practical numerical implementation, the potential contact area is discretized into a grid of elements. The elastic displacements at each element are calculated superimposing the influence of all the elements in the contact area, and the contact conditions are checked at each of the elements. Due to the fact that the problem has to be solved iteratively and that a system of coupled equations is involved, the computational costs of this contact model are relatively high as compared with other simplified rolling contact models. In past decades, its application for online rail vehicle MBS dynamic simulations was considered impractical due to the high computational costs. However, nowadays this has become feasible thanks to recent advances [25,26].

The extension of the exact rolling contact theory from its usual form for application in non-conformal contacts, to conformal contact, comprises the following aspects:

- Normal undeformed distances: in many simplified rolling contact models, a quadratic form of the undeformed distance function is assumed in the rolling direction, see Refs. [16,27] for example. However, with conformal contact, this may result in high inaccuracies, especially with high contact angles and yaw angles. In some cases, it may not be accurate to represent the undeformed distance with quadratic variation in the rolling direction and constant transverse undeformed distance profile even with zero mean contact and yaw angles, as will be shown later.
  In the developed extension of the exact rolling contact theory, the normal undeformed distances are computed in a rigorous way at each point in the contact. For this purpose, the intersection of both contacting bodies with planes orthogonal to the x direction is computed at all the positions of the contact mesh. The normal undeformed distance is calculated at each lateral position as the projection of the position difference vector between homologous points in both contacting bodies, over the local normal direction of the surface of the potential contact area. Homologous points are defined as points having the same longitudinal x and lateral s coordinates in the local contact coordinate system.
- Rigid slip velocities: with non-planar contact areas, it is no longer possible to calculate the rigid slip velocities throughout the contact patch from a single set of creepages, typically of the rigid contact point, as can be done with planar contact areas. In this work they are calculated as the projection of the relative rigid velocity vector between the two contacting bodies, on the tangent plane in each position of the potential contact area.
- Influence coefficients: the ICs characterize the mechanical response of the solids in contact near the contact area. Here they are defined as the response of the elastic bodies in terms of surface displacements, to distributed tractions applied over an element of the contact surface mesh. In the case of punctual contact between homogeneous, isotropic and linear elastic bodies, it can be assumed that the contacting bodies behave like elastic half-spaces around the contact, which is very convenient because the influence functions of the elastic half-space can be analytically calculated, are not specific for each contact problem, and are readily available in the literature, see Ref. [15] for example.

This last assumption is implicit in most of the rolling contact models used nowadays, but with conformal geometries it becomes questionable. In Ref. [23] it was shown that the B_{sn} ICs (i.e. the displacements along the s direction due to tractions applied in the n direction) play an important role in the tangential part of the contact problem, and that the B_{sn} ICs computed for the half-space can deviate significantly from the true B_{sn} ICs for non-planar geometries. Consequently, the results in the tangential part of the contact problem can be substantially degraded even with low to moderate total contact angle variations in the contact patch. Here it will be shown that for higher total contact angle variations, the results in the normal part of the contact problem are also compromised if the B_{nn} ICs for the half-space are used.

Therefore the need to compute the ICs with more precision for conformal or non-planar geometries arises. However, this represents a considerable hindrance, since in general they have to be computed numerically for each particular geometry. In order to overcome this difficulty, in Ref. [23] a simple approximation was proposed, based on combining the ICs for the half-space according to the decomposition of the applied tractions along the principal directions of each point in the contact. That is, the applied tractions are decomposed into a normal and a lateral tangential component at each point, and the contribution due to each of these components is approached with the corresponding half-space IC. Thus, a different decomposition of the applied tractions is carried out at each lateral position of the non-planar potential contact area, depending on the difference in orientation between the position where the traction is applied and each lateral position of the potential contact area. In this work this same approximation is used. As was shown in Ref. [23], with this approximation the results in the tangential part of the contact problem are markedly improved. In that work, a remarkable accuracy improvement was shown in the computed B_{sn} ICs for a convex body with circular geometry in its cross section. In Figs. 2 and 3 other geometries are tested. In Fig. 2 a body with double curvature is considered, having a central concave zone delimited by two convex zones in its cross section, and in Fig. 3 a body with elliptical geometry in its cross section is considered, with a major semi-axis of 20 mm and 2:1 semi-axes ratio (with its major semi-axis oriented in the vertical direction). In both cases, the load is applied uniformly distributed on a rectangle of longitudinal dimension of 0.24 mm and lateral dimension of 0.21 mm approximately, centred in the lateral plane of symmetry of the bodies. The surface displacements are observed along the lateral curvilinear s coordinate on the surface of the bodies, in a cross section 0.24 mm away from the centre of the loaded rectangle. The curvilinear s coordinate is orthogonal to the x direction, and its origin is taken to be at the lateral plane of symmetry of the bodies in these cases.

As can be seen in Figs. 2 and 3, although with these geometries the proposed approximation is somewhat less accurate (especially in the body with the abrupt change in curvature of Fig. 2), it is still reasonably good, and provides a much better representation of the true ICs of these non-planar geometries than the half-space ICs.

3. Results

Situations with varying conformity levels are analyzed, with the presented FE models and with CECT. The Hertzian theory and CECT neglecting some aspect of conformity will be used as well, with the purpose of showing the errors that result with these simplifications. In order to better illustrate the particular features of conformal contact, geometries as simple as possible are studied, considering bodies with constant curvatures in the contact, in situations with zero mean contact angles and yaw angles. Specifically two different cases will be considered, with different ratios of the longitudinal to the lateral dimensions of the resulting contact patches. The relevant geometric parameters of both cases considered, named as Case 1 and Case 2, are listed in Table 1.

In Table 1, R_{yr} and R_{yw} designate the transversal curvature radii of the rail and the wheel respectively, and R_{xw} the rolling radius of the wheel at the first point of contact. Convex curvatures are defined with positive
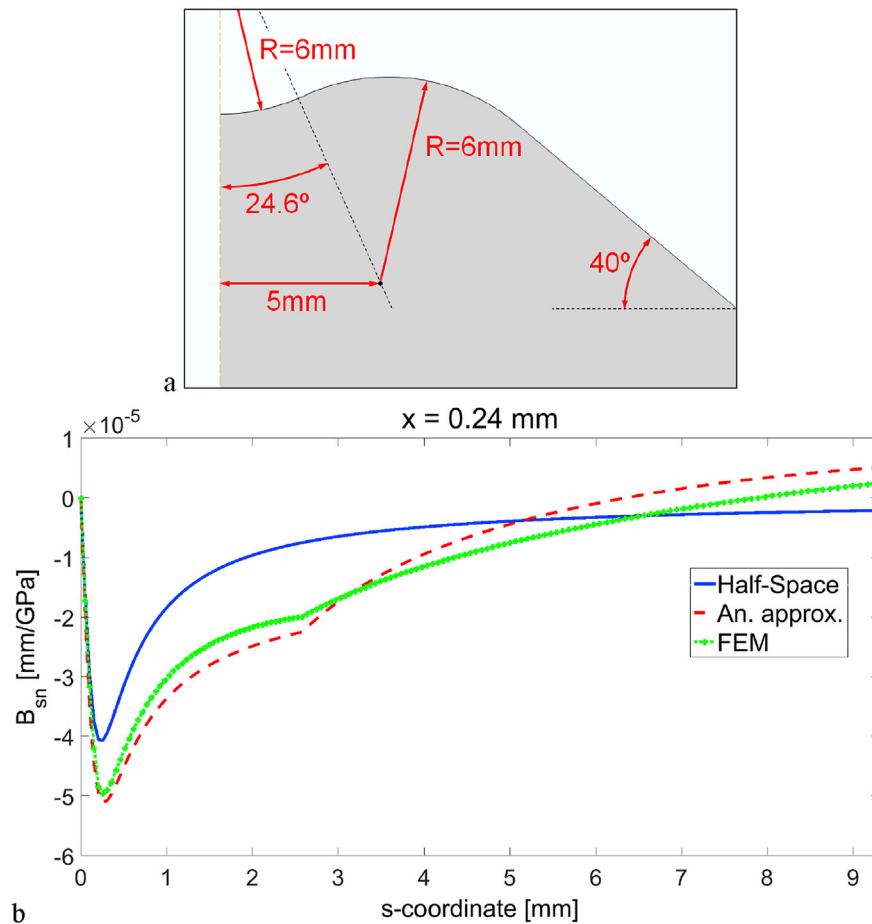
Fig. 2. Comparison of B_{sn} ICs for the half-space and for a non-planar prismatic body with double (concave and convex) curvature in its cross section. (a) Cross section of the body (only part of one of the halves of the symmetric cross section is shown) and (b) B_{sn} ICs (anti-symmetric about $s = 0$). Blue solid line: half-space. Red dashed line: proposed analytical approximation for non-planar geometries. Green dotted line with + marks: computed with FEM. (For interpretation of the references to colour in this figure legend, the reader is referred to the web version of this article.)

sign, and concave curvatures with negative sign. $(a/b)_{Hz}$ is the ratio of the longitudinal to the lateral dimension of the Hertzian contact ellipse in each case.

The contact surfaces are considered to be smooth, with no roughness, and the material of both contacting bodies is assumed to be steel, with isotropic and linear elastic behaviour. The following elastic properties are considered for the material: shear modulus of 81 GPa, and Poisson's ratio of 0.30.

3.1. Frictionless contact

In this section the normal part of the contact problem is studied, assuming frictionless contact, for the two cases described above. Even in these simple cases, a simple Hertzian calculation will not provide precise results with sufficiently high total contact angle variations in the contact patch. For example, in Case 2, when the total contact angle variation in the contact patch reaches around 60°, the contact patch width predicted with the Hertzian theory is around 10% higher than the reference computed numerically. However, the Hertzian results can be considerably improved applying a geometric correction as shown next. For this, the influence of the rigid approach between the contacting bodies on the resulting normal undeformed distance has to be considered. The reason is that this influence is variable across the width of the contact patch, because it is multiplied by a cosine term according to the difference in orientation between the direction along which the approach takes place, and the normal direction at each point in the contact patch. The relationship between the normal undeformed distance before and after

application of the approach is expressed in Eq. (1) and depicted schematically in Fig. 4, with h_d and h being the normal undeformed distances after and before the application of the approach respectively, d the approach, and α the angular difference between the direction of the approach and the direction of the local normal at each point in the contact patch.

$$h_d = h - d \cos(\alpha) \tag{1}$$

Even with quite high total contact angle variations in the contact patch, in the simple cases considered here the normal undeformed distance h can be expressed to a first order approximation according to Eq. (2):

$$h = A \cos(\alpha) x^2 + B s^2 \tag{2}$$

In Eq. (2), x and s are the longitudinal and lateral coordinates in the local reference system, being the point (0, 0) the rigid point of contact; and A and B are respectively the longitudinal and lateral curvatures of the normal undeformed distance, calculated in the usual way according to the longitudinal radii of curvature r_{x1} and r_{x2} and the lateral radii of curvature r_{y1} and r_{y2} of the two bodies in contact as shown in Eq. (3):

$$A = (1/r_{x1} + 1/r_{x2}) / 2 \tag{3}$$

$$B = (1/r_{y1} + 1/r_{y2}) / 2$$

In this equation, convex curvatures have to be taken as positive, and concave curvatures as negative. Next, the expression in Eq. (2) for h is
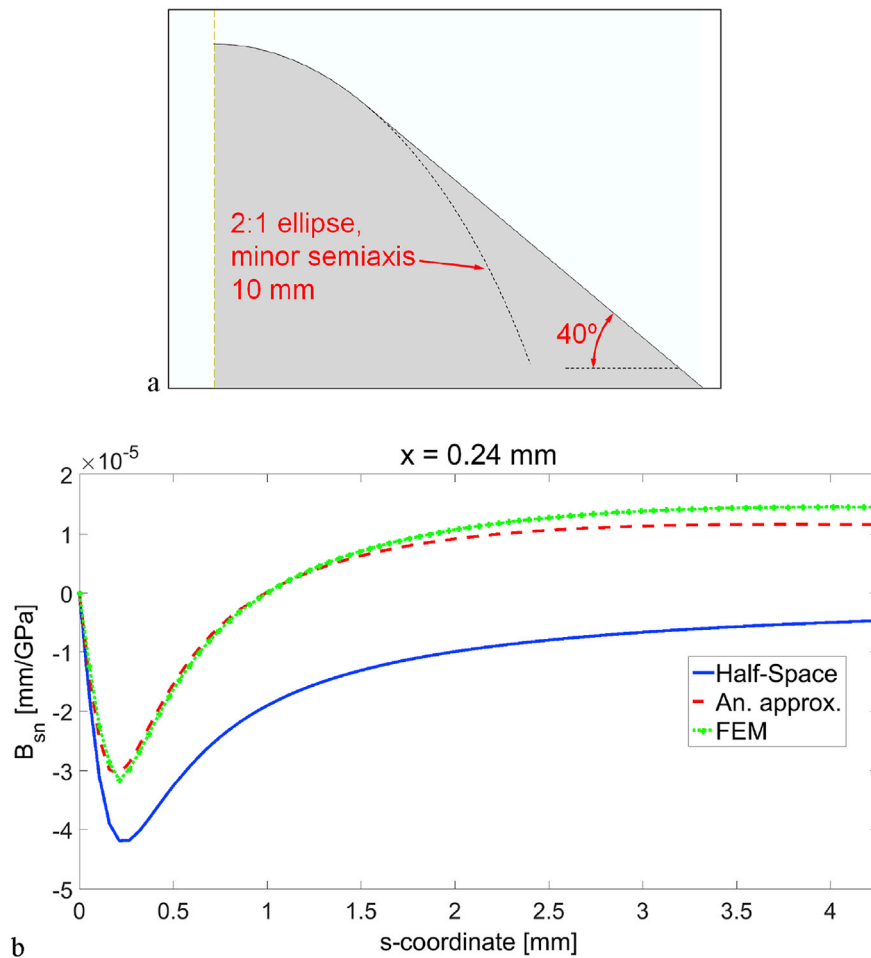
Fig. 3. Comparison of B_{sn} ICs for the half-space and for a non-planar prismatic body with elliptical geometry in its cross section. (a) Cross section of the body (only part of one of the halves of the symmetric cross section is shown) and (b) B_{sn} ICs (anti-symmetric about $s = 0$). Blue solid line: half-space. Red dashed line: proposed analytical approximation for non-planar geometries. Green dotted line with + marks: computed with FEM. (For interpretation of the references to colour in this figure legend, the reader is referred to the web version of this article.)

Table 1
Geometric parameters of the studied cases.

	Case 1	Case 2
R_{yr} [mm]	10.0	10.0
R_{yw} [mm]	−10.1	−10.5
R_{xw} [mm]	500.0	653.7
$(a/b)_{Hz}$ [−]	0.63	2.13

Fig. 4. Cross section of two bodies in conformal contact showing the normal undeformed distance before and after application of the approach.

substituted in Eq. (1). Taking the series expansion of the cosine function, neglecting higher order terms and rearranging, Eq. (4) is obtained.

$$h_d = A \cos(\alpha)\, x^2 - d + (B + d/2r^2)\, s^2 \tag{4}$$

In Eq. (4), r is the mean radius of curvature of the final contact surface, which with identical materials in contact can be taken as the mean of the absolute values of the lateral radii of curvature r_{y1} and r_{y2} of both bodies in contact. In view of Eq. (4), a corrected B coefficient, B_{corr}, for the undeformed distance may be defined as:

$$B_{corr} = B + d/2r^2 \tag{5}$$

The approach d needed in Eq. (5) to compute the corrected B_{corr} coefficient, may be obtained from a usual Hertzian calculation. The second term in the right hand side of Eq. (5) is negligible in non-conformal contact, but in conformal contact it can easily be of the same order of magnitude as B or higher. Therefore, it is seen that in conformal contact the effective lateral curvature of the undeformed distance function around the contact is increased with the approach or the load.

The most representative results of the normal contact problem, obtained with different contact models, are plotted as a function of the applied load in Figs. 5 and 6, for Cases 1 and 2 respectively. The results shown in the figures are the maximum normal pressure, the total contact angle variation $\Delta\delta$, the ratio of the longitudinal to the lateral dimensions of the contact patch (which will be also referred to as a/b ratio in order to abbreviate) and the approach. The models described in the previous
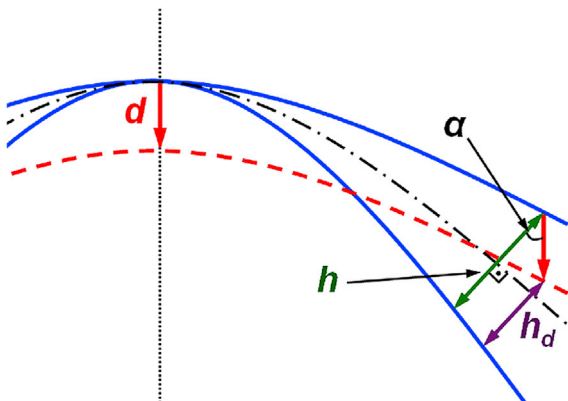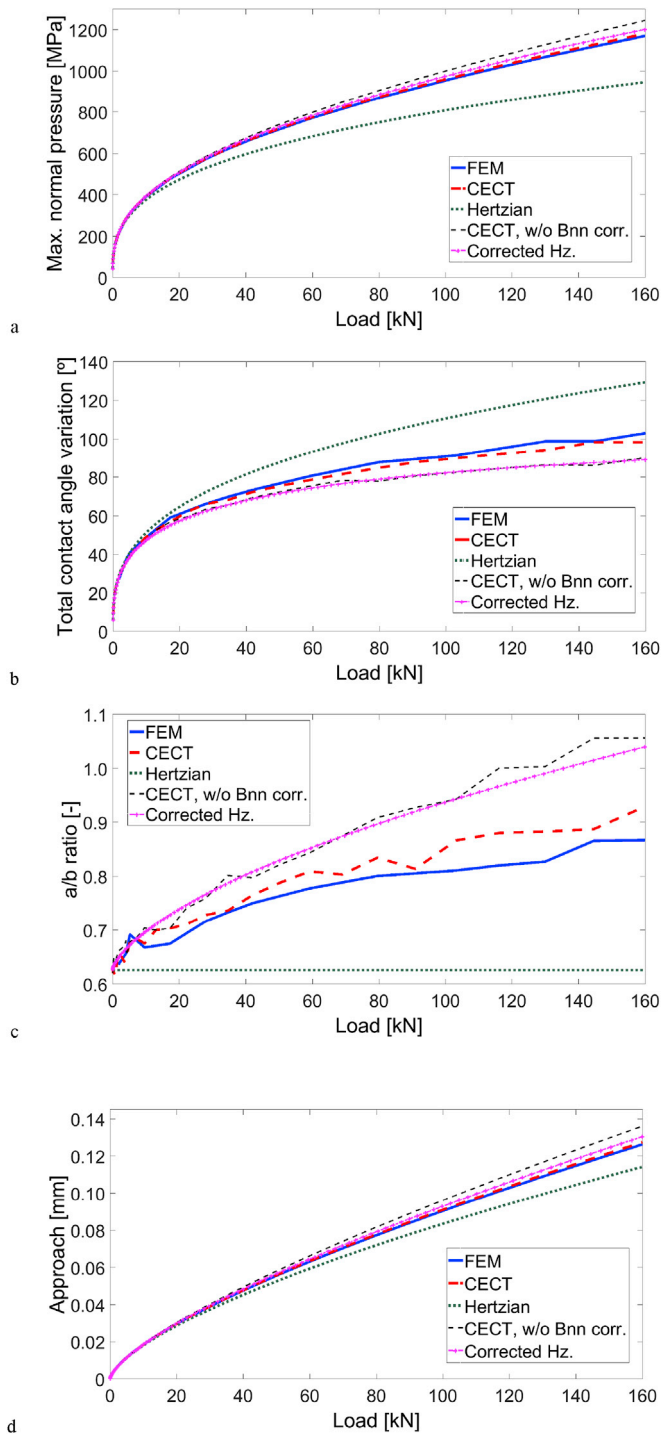
Fig. 5. Main results of normal contact problem for Case 1 with different analysis methods as a function of the applied load. (a) Maximum normal pressure. (b) Total variation of contact angle in contact patch. (c) Ratio of longitudinal to lateral dimensions of contact patch. (d) Approach. FEM results in solid, thick blue lines; results from CECT in dashed, thick red lines; Hertzian results in dotted, thick green lines; results from CECT with ICs of the half-space in dashed, thin black lines; and corrected Hertzian results in dash-dotted, thin magenta lines with + marks. (For interpretation of the references to colour in this figure legend, the reader is referred to the web version of this article.)
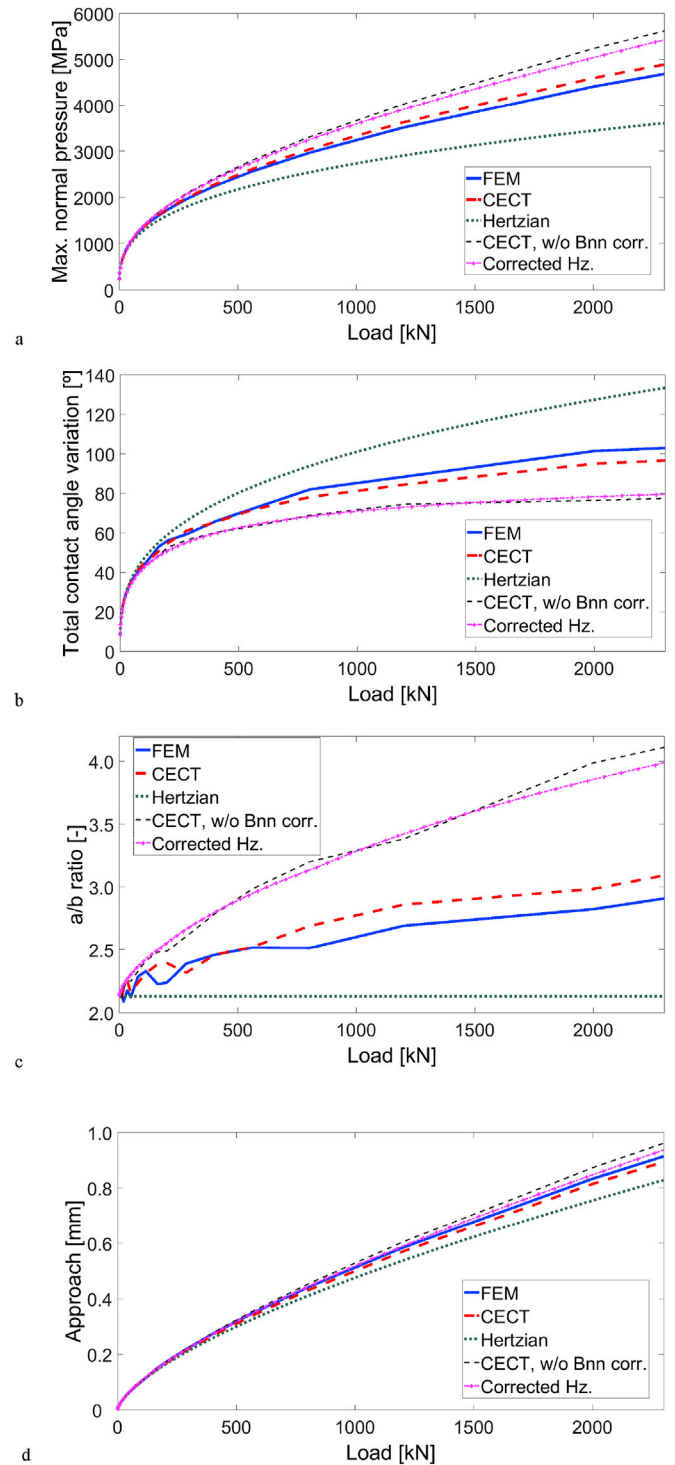
Fig. 6. Main results of normal contact problem for Case 2 with different analysis methods as a function of the applied load. (a) Maximum normal pressure. (b) Total variation of contact angle in contact patch. (c) Ratio of longitudinal to lateral dimensions of contact patch. (d) Approach. FEM results in solid, thick blue lines; results from CECT in dashed, thick red lines; Hertzian results in dotted, thick green lines; results from CECT with ICs of the half-space in dashed, thin black lines; and corrected Hertzian results in dash-dotted, thin magenta lines with + marks. (For interpretation of the references to colour in this figure legend, the reader is referred to the web version of this article.)

section have been used (i.e. FEM models and the exact contact theory extended for conformal contact or CECT), as well as the Hertzian theory. Additionally, results have been computed also with CECT, but without performing any correction of the ICs for non-planar geometries (i.e. using directly the half-space B_{nn} ICs, with no correction), and also with the Hertzian theory performing the correction in the lateral curvature of the undeformed distance in the contact as described above.

As can be seen in Fig. 5, in Case 1 the agreement between the FEM and CECT is very good. The errors in the maximum contact pressure and in the approach are limited to less than 1% in the whole range of contact angle variations studied, up to a $\Delta\delta$ of about 100°. The precision in the results directly related to the contact patch dimensions (i.e. $\Delta\delta$ and the a/b ratio) computed with the numerical models is limited by the resolution provided by the used discretization, which has been on the order of 50 elements at most in the lateral direction (i.e. about 25 elements in each half of the contact patch). So, the resolution in the computed dimensions of the contact patch is limited to around 4%. This is the reason of the noise seen in the trends of these results computed with FEM and with CECT. Nevertheless, the differences in the computed $\Delta\delta$s with FEM and with CECT remain below 5% in the whole range of $\Delta\delta$s studied. The differences in the a/b ratios are a bit higher with $\Delta\delta$s above 80°, reaching around 7% with a $\Delta\delta$ of around 100°. The contact patches computed with CECT are somewhat narrower than those computed with FEM. The differences in the computed contact patch areas (not shown in these figures) are lower, below 2%, the areas computed with FEM being slightly higher than those computed with CECT.

The effect of the ICs may be appraised by comparing the results computed with CECT using the ICs of the half-space, with those computed with FEM and with CECT using the proposed analytical approximation of the ICs for non-planar geometries. In order to isolate the effect of the ICs, differences between the results computed with both used versions of CECT (i.e. with the half-space ICs on the one hand, and with the proposed analytical approximation of the ICs for non-planar geometries on the other hand) are quoted next. For the normal part of the contact problem, in Case 1 it is seen that with $\Delta\delta$s of up to about 40° (which corresponds to a load of about 5 kN for this case as can be seen in Fig. 5b), the use of the half-space ICs is satisfactory, the errors in the computed maximum pressures and approaches being below 1%. However, as $\Delta\delta$ increases, the errors introduced by this simplification become more appreciable, increasing to about 5.5% and 6.8% in the maximum pressure and approach respectively in the case with the highest $\Delta\delta$. Using directly the half-space ICs without any correction, the computed contact patches are narrower, with higher maximum pressures, and the approaches are higher. The reason for this is that, with conformal geometries –and identical materials in contact-, as the lateral angular difference in orientation between any two points increases, the real B_{nn} IC between those points (i.e. the IC relating the displacement along the normal direction at one point due to the normal pressure on the other point) is lower than the half-space B_{nn} IC. As a result, using the half-space B_{nn} ICs, the elastic displacements caused at different points in the contact patch by points located at different orientations will be overestimated, and thus will be the computed approach. By the same reason, the elastic displacements at the sides of the contact patch caused by the normal pressures acting on the central part will also be overestimated, so that, in order to maintain compatibility in the normal contact conditions, the normal pressures sustained at the sides of the contact patch will decrease, and those sustained at the central part will necessarily increase in order to maintain equilibrium. Therefore the net effect is that in conformal contacts, there is a lateral spreading effect associated with the real elastic behaviour of non-planar geometries; i.e. the load is more effectively shared between the different longitudinal strips of the contact patch, and the contact patch is more spread in the lateral direction than predicted with the use of the half-space ICs.

Referring to the Hertzian results, these are seen to provide quite accurate results in Case 1 for $\Delta\delta$s of up to about 40°. With this $\Delta\delta$, the errors in the computed maximum pressure and approach are around 2.6% and

2.0% respectively with respect to the reference FEM results. And with a $\Delta\delta$ of 103° in the lateral direction, these errors increase to 19% and 9.6% respectively. With this $\Delta\delta$, the corresponding errors in the contact angle variation and in the a/b ratio are of 26% and 28% respectively. As seen in Fig. 5, with the Hertzian calculation the maximum pressure, approach and a/b ratio are underestimated, and the contact angle variation is overestimated.

Performing the correction in the lateral curvature of the undeformed distance as explained above, a notable improvement is achieved in the Hertzian results. For a $\Delta\delta$ of around 100°, the errors in the maximum pressure, approach, contact angle variation and ratio of longitudinal to lateral contact patch dimensions, decrease from the mentioned values to 2.7%, 3.3%, 13% and 20% respectively, and have the opposite sense: the maximum pressure, approach and a/b ratio are overestimated, and the contact angle variation is underestimated. It is remarkable that the contact pressures and approaches computed with the corrected Hertzian calculation, are even more precise than those computed with CECT using the half-space ICs. This is explained because of two sources of error that are partially counteracting each other in the corrected Hertzian calculation. On the one hand, as a result of the half-space elastic behaviour which is implied in the Hertzian calculation, the maximum pressures and approaches tend to be overestimated, as explained above. On the other hand, the approach d from the pure Hertzian calculation that is used to calculate the corrected lateral curvature of the undeformed distance according to Eq. (5), is lower than the real value as seen in Fig. 5d. Therefore the computed lateral curvature of the undeformed distance is lower than the real one, and this has the effect of decreasing both the computed approaches and maximum pressures.

In Case 2, the agreement between the results computed with FEM and with CECT is not as good as in Case 1, as can be seen in Fig. 6. For example, with a $\Delta\delta$ of 101° computed with FEM, the differences in the maximum normal pressures and approaches computed with both models are of 4.2% and 2.2% respectively, while in Case 1 they were below 1% as mentioned earlier. At the same time, also higher discrepancies are encountered between the results computed with CECT using the approximation of the ICs for non-planar geometries on the one hand, or directly those of the half-space on the other hand. In the case with a $\Delta\delta$ of 101°, the difference in the computed maximum pressure with both versions of CECT is of 14%; cf. the difference quoted earlier for Case 1, of 5.5%. The reason for the increased discrepancies seen in Case 2, between the FEM results and CECT as well as between the two versions of CECT with different ICs, lies on the fact that as the contact patch becomes more elongated in the longitudinal direction, the relative contribution to the elastic displacements at different points in the contact patch becomes more spread across the lateral direction of the contact patch. In order to show this, in Fig. 7 the unitary contribution of the normal pressures acting on each longitudinal strip of the contact patch to the normal elastic displacement of a point located in the lateral part of the contact patch, for different a/b ratios of the contact ellipse in Hertzian contact, are plotted.
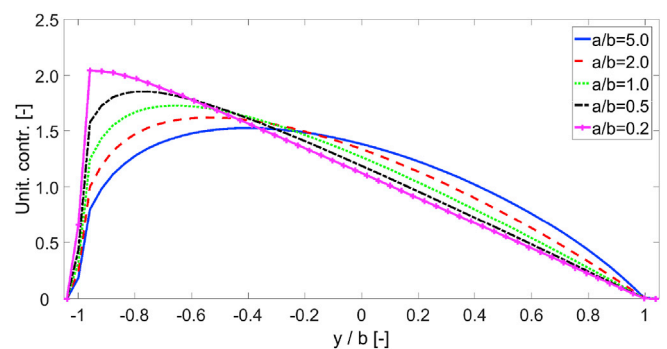
Fig. 7. Unitary contribution of each longitudinal strip of the contact patch to the normal displacement at the central point of the left lateral strip, for Hertzian cases with fixed lateral b semi-axis and different longitudinal to lateral (a/b) semi-axis ratios.

As can be seen in Fig. 7, at higher a/b ratios these contributions become more spread across the contact patch. Therefore, with more elongated contact patches it is more important to characterize accurately the lateral variation of the ICs. For this same effect, which also happens in non-conformal contact, the improvement gained with the corrected Hertzian calculation in Case 2 is more limited than in Case 1.

Next, the contact patch contours for both cases considered in this Section are shown in Fig. 8, for different $\Delta\delta$s in the contact patch, plotted in nondimensional axes. The longitudinal x and lateral s coordinates are nondimensionalized dividing them by the corresponding maximum coordinates of the contact patch in each direction, x_{max} in the longitudinal direction and s_{max} in the lateral direction. The reference elliptic contour for the non-conformal case is also shown in the figures. As $\Delta\delta$ increases, the resulting contact patches deviate from the non-conformal elliptic shape, changing towards a more rectangular-like shape. This can be explained by the geometry of the undeformed distance function. As indicated in Eq. (4), the longitudinal curvature decreases in the lateral parts of the contact area due to the multiplication by the cosine term, and due to this the longitudinal dimension of the strips in the lateral parts of the contact area tends to increase.

3.2. Frictional static contact

In this Section as well as in the next Section 3.3, the frictional behaviour in the contact interface is modelled using Coulomb's law, with a constant static and kinetic coefficient of friction of 0.30. Here, the same two cases of Section 3.1 are considered. As before, the static compression between both contacting bodies is computed, but this time with friction added in the interface. Starting from zero load, a monotonically increasing compressive load is imposed between the two contacting bodies, with no tangential shifts.

Fig. 9 shows the lateral distributions of lateral tangential stress p_s across the middle section of the contact patch, for different $\Delta\delta$s, computed both with FEM and with CECT. The tangential stresses are nondimensionalized in the figure dividing them with the maximum traction bound (i.e. the maximum normal pressure p_{nmax} multiplied by the coefficient of friction μ) in each case, and the nondimensional values of the abscissa axes of the graphs are the lateral s coordinates divided by the maximum s coordinate in the contact patch in each case. The results used to nondimensionalize the variables are those computed with FEM, except for the cases with lowest $\Delta\delta$s, where the results computed with CECT have been used. Only one half of the section is shown, as the tangential stresses are anti-symmetric with respect to $s = 0$. Additionally, the curves of nondimensional normal pressure at the same cross section computed with FEM are also shown in the figure, for the situations with the highest $\Delta\delta$ in each case, with an approximate $\Delta\delta$ of 100°, both

considering friction in the interface as explained above, and for equivalent frictionless cases. The normal pressures are nondimensionalized dividing them by the maximum normal pressure in each case.

Qualitatively the results are similar in both cases, and apart from the noise in the numerical solutions the agreement between the results obtained with the FE models and with CECT is good. This good agreement is maintained in the contours of the adhesion and slip zones, depicted in Fig. 10 for the situations with the highest $\Delta\delta$ in each case. As can be seen in Fig. 10, the width of the adhesion zone, located in the centre of the contact patch, is nearly constant along the contact patch, with the boundary between the adhesion and slips zones being nearly parallel to the longitudinal direction both in Case 1 and in Case 2. The relative width of the adhesion zone decreases, and the magnitude of the tangential stresses increases with $\Delta\delta$. Evidently, a purely non-conformal contact model would not capture these tangential stresses.

Regarding the normal pressures, as can be seen in Fig. 9 there are appreciable differences between the distributions of normal pressures obtained with and without friction, the maximum normal pressures tending to decrease with friction in the interface. As explained in Ref. [23], this is due to the coupling between the normal and the tangential parts of the contact problem, which happens in conformal contact in spite that the materials of both contacting bodies are elastically identical. This leads to a difference in the maximum normal pressure between the frictional and the frictionless cases of 6.3% in Case 1, and 8.9% in Case 2. The coupling between the normal and the tangential parts of the contact problems happens at two levels: on the one hand, at the level of the global equilibrium equations as explained in Ref. [18], due to the fact that the tangential stresses sustain part of the normal load; and on the other hand at the purely contact mechanics level, via the B_{ns} ICs as explained in Ref. [23]. This coupling is stronger in Case 2 than in Case 1, due to the higher cross-influence between different longitudinal strips of the contact patch with more elongated contact patches, as depicted in Fig. 7. It has to be mentioned that in order to be able to make a more direct comparison between the frictional and the frictionless cases, the total normal load has been adjusted in the frictionless cases, so that the resultant of the normal pressures is the same that in the frictional cases (i.e. the total normal load is higher in the frictional cases, due to the contribution of the tangential stresses). Therefore, the differences in the maximum normal pressures are entirely due to the coupling via the B_{ns} ICs. In the frictional cases, the proportion of the normal load sustained by the tangential stresses amounts to 8.9% of the total normal load in Case 1, and to 8.5% in Case 2.

3.3. Rolling contact

In this Section the laterally symmetric steady state rolling contact, with zero yaw angle and lateral creepage, is studied with the geometry of Case 1 of Table 1. The normal load is 80 kN, and the resulting $\Delta\delta$ is about 88°. In order to describe the different rolling contact scenarios, the creepage term inherited from non-conformal contact is used here. In this context, the creepage is defined according to the rigid slip velocities applied at the rigid or central contact point. In the following subsections, different aspects of the tangential part of the rolling contact problem are discussed.

3.3.1. Tangential stresses and slip velocities

To start with two situations are considered, one of them of braking rolling and the other of tractive rolling. In both situations the yaw angle and the lateral creepage are zero. The tangential traction distributions and contours of adhesion and slip zones computed both with FEM and with CECT are shown in Fig. 11 for the situation of braking rolling contact, and in Fig. 12 for the situation of tractive rolling contact. The rolling takes place in the positive x direction of the figures. In order to make a more representative comparison between the results computed with the two types of models, the longitudinal creepages are adjusted in each case in order to obtain the same longitudinal resultant force with
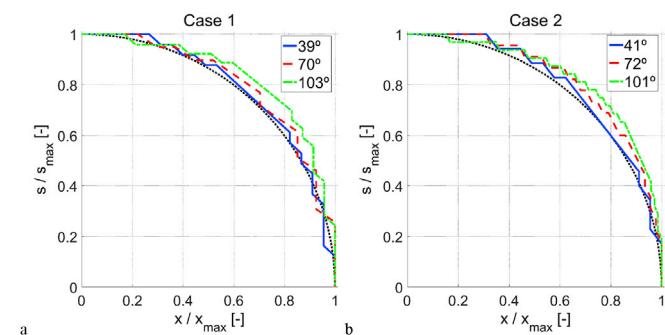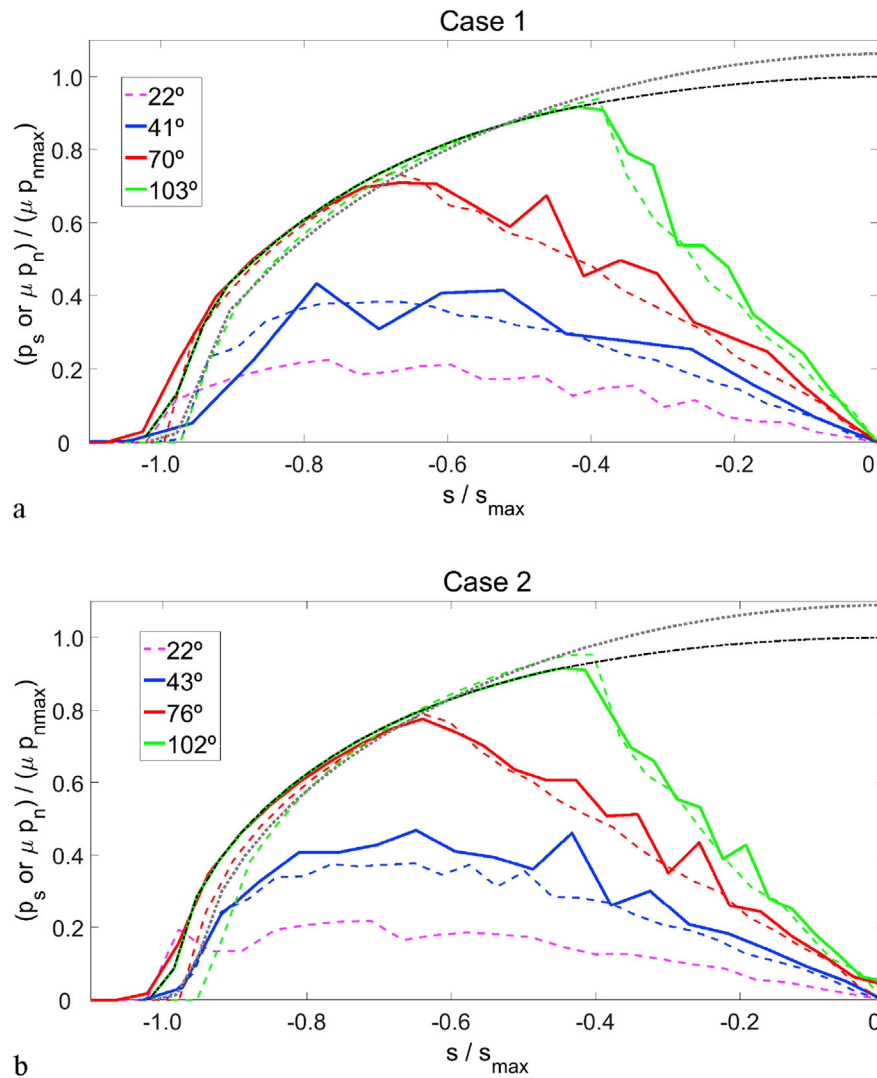

Fig. 8. One quarter of the contact patch contours (symmetric in the lateral and in the longitudinal directions about $s = 0$ and $x = 0$ respectively) obtained in Cases 1 (a) and 2 (b) for approximate $\Delta\delta$s of 40°, 70° and 100°, plotted in nondimensional axes. 40°: solid blue lines. 70°: dashed red lines. 100°: dash-dotted green lines. Elliptic contour shown in thin, black dotted lines. All results computed with FEM except for the case with a $\Delta\delta$ of 39° in Case 1, which has been computed with CECT. (For interpretation of the references to colour in this figure legend, the reader is referred to the web version of this article.)

Fig. 9. Nondimensional lateral tangential stress across the middle section of the contact patch in static compression with monotonically increasing load, for approximate $\Delta\delta$s of 22° (in magenta lines), 40° (in blue lines), 70° (in red lines) and 100° (in green lines). a) Case 1. b) Case 2. Results computed with FEM in solid lines and results computed with CECT in dashed lines. Nondimensional normal pressure for the case with an approximate $\Delta\delta$ of 100°, with friction in black dash-dotted lines, and without friction in grey dotted lines. Lateral tangential tractions p_s anti-symmetric about $s = 0$, and normal pressures p_n symmetric about $s = 0$. (For interpretation of the references to colour in this figure legend, the reader is referred to the web version of this article.)

both models. In the braking rolling contact case shown in Fig. 11, the resultant unitary longitudinal contact force, defined as the resultant longitudinal force F_x divided by the product of the coefficient of friction μ

and the normal load F_n, is −0.27. The longitudinal creepage applied in the FEM analysis is −0.2%, and that applied in the analysis with CECT is −0.153%. In the tractive rolling contact case shown in Fig. 12, the
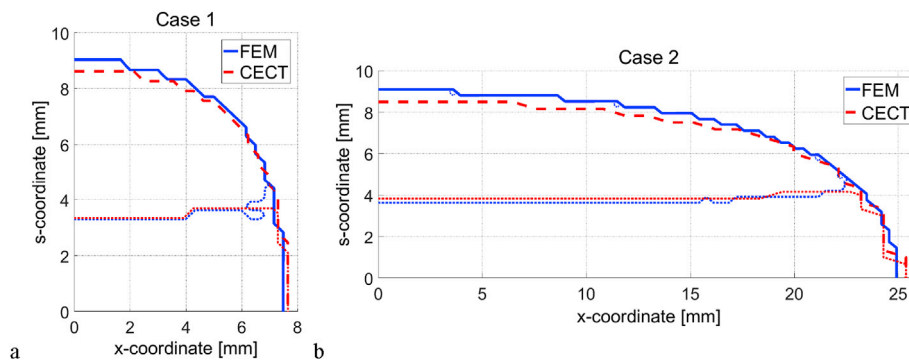

Fig. 10. One quarter of the contact patches (symmetric in the lateral and in the longitudinal directions about $s = 0$ and $x = 0$ respectively) with contours of adhesion and slip zones computed for the case with an approximate $\Delta\delta$ of 100°, for Case 1 (a) and Case 2 (b). Results computed with FEM in blue lines (limits between interior and exterior areas in thick solid lines, and limits between adhesion and slip areas in thin dotted lines), and results computed with CECT in red lines (limits between interior and exterior areas in thick dashed lines, and limits between adhesion and slip areas in thin dotted lines). (For interpretation of the references to colour in this figure legend, the reader is referred to the web version of this article.)
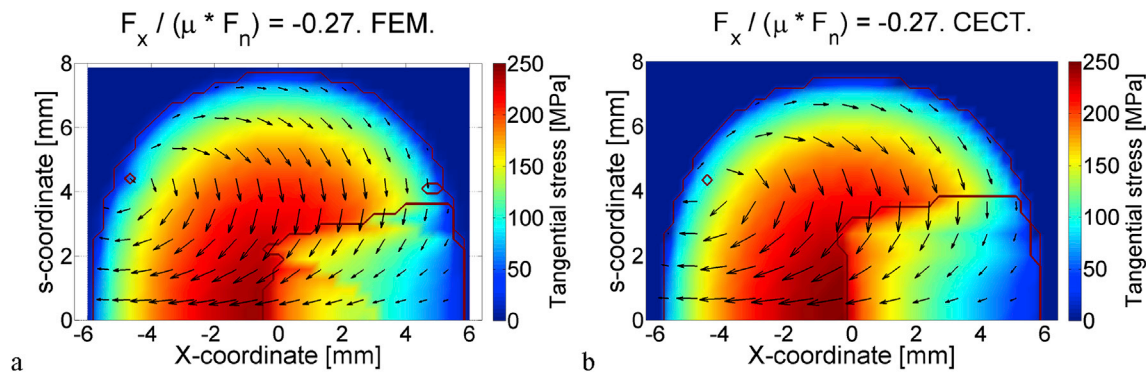
Fig. 11. Tangential traction distributions and contours of adhesion and slip zones in conformal, braking rolling contact with zero mean contact angle, zero yaw angle and zero lateral creepage, computed with FEM (a), and CECT (b). Only one half of the contact patch is shown, the results being symmetric about the longitudinal centreline.
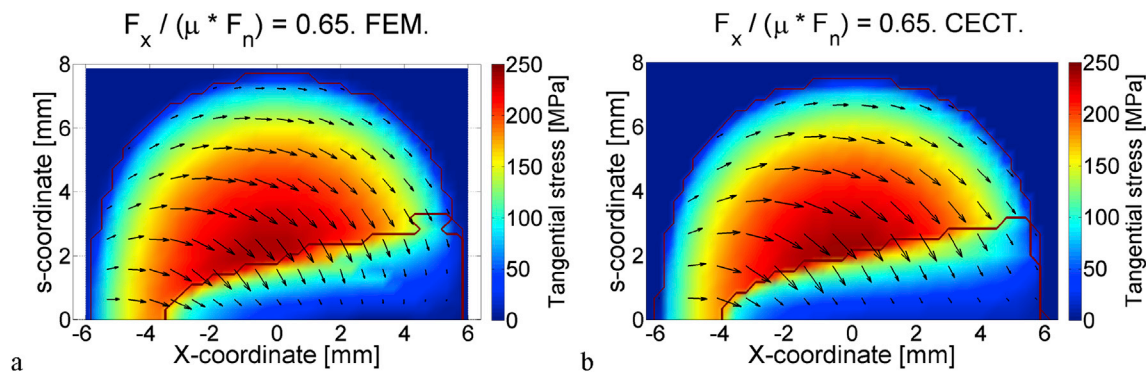

Fig. 12. Tangential traction distributions and contours of adhesion and slip zones in conformal, tractive rolling contact with zero mean contact angle, zero yaw angle and zero lateral creepage, computed with FEM (a), and CECT (b). Only one half of the contact patch is shown, the results being symmetric about the longitudinal centreline.

resultant unitary longitudinal contact force is 0.65, and the longitudinal creepages applied in the analyses with the FEM and with CECT are 0.05% and 0.086% respectively.

In the two cases shown in Figs. 11 and 12 the tangential stresses have a variable direction across the contact patch, due to the variable contact angle and associated geometrical spin. In the tractive case of Fig. 12, the positive creepage adds to the effect of the increasing rolling radii away from the central longitudinal slice of the contact area, while in the braking case of Fig. 11 the effects are in opposite senses. As a result, the way in which the rigid slip velocities vary throughout the contact patch is different in each case. The net effect is that the adhesion zone tends to become more extended in the lateral direction in the braking case, and it becomes more acute shaped in the tractive case. In both situations, the lateral zones of the contact patch, with a high contact angle and high associated geometrical spin, are sliding, and remain so not only in the two particular situations shown here, but in the whole range of longitudinal creepages. It is observed as well that the adhesion zone is less extended in the longitudinal direction in the braking case than in the tractive one, even though the resultant longitudinal force is smaller in the braking case. This is due to the fact that the absolute value of the creepage is higher in the braking case, cf. the creepage values for both cases quoted above. Despite the higher absolute value of the creepage in the braking case, the resultant longitudinal force is smaller than in the tractive case, due to the contribution of the most lateral longitudinal slices of the contact patch, which, as a result of the higher rolling radii at these zones, is tractive.

3.3.2. Frictional work

In some contact wear models, wear is assumed to be directly related to the frictional work density, see e.g. Ref. [28]. Therefore, this magnitude is of primary interest in the study of wear in the contact interface. In

Fig. 13 the lateral distributions of the frictional work in the rail after a wheel passage W_{fric}, computed with FEM, are depicted for several cases with varying longitudinal creepages. The abscissa axis of the graph of the figure spans only one half of the contact patch width, as the results are symmetric about $s = 0$. Starting with the case with the highest braking (i.e. negative) longitudinal creepage shown in the figure, the maximum frictional work density is clearly located in the central part of the contact patch, due to the fact that both the highest tractions and slip velocities are located in this part. On the other hand, at not too high braking longitudinal creepages, a relative maximum in the lateral distribution of the frictional work density begins to appear in the sides of the contact area, associated to the increasing slip velocities in those parts.
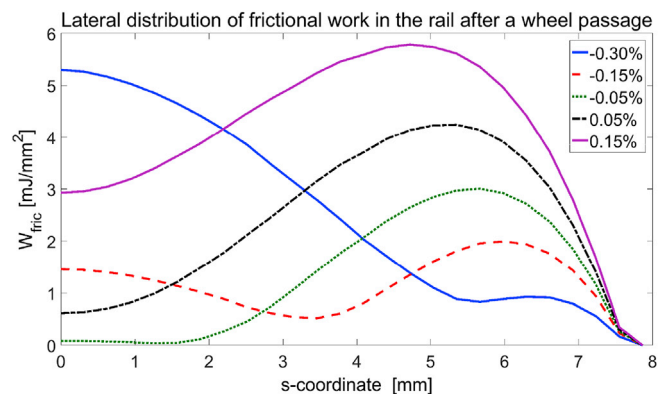

Fig. 13. Lateral distribution of integrated frictional work in the rail after a wheel passage, in conformal rolling contact with zero yaw angle and lateral creepage, for different values of longitudinal creepage as shown in the legend of the figure. Results computed with FEM (symmetric about $s = 0$).

As the longitudinal creepage increases towards the tractive regime, the frictional work density in the central part of the contact patch initially decreases, while it increases in the sides, because the slip velocities are decreasing in the central part, and increasing in the sides of the contact patch. With a longitudinal creepage of -0.05%, the frictional work almost vanishes in the central part of the contact patch in roughly one quarter of its width, as the contact patch is in adhesion along most of its length in that part. With this longitudinal creepage, the resultant unitary longitudinal contact force is already tractive, with a value of 0.30.

As the longitudinal creepage increases further into the tractive regime, the frictional work increases in the whole width of the contact patch, due to the general increase of the slip velocities in the contact patch, while the position of the maximum frictional work density gradually moves towards the central strip of the contact patch. At sufficiently high positive creepages, the maximum frictional work density will be located again in the central part of the contact patch, where the maximum contact stresses are located. Nevertheless, in a wide range of longitudinal creepages, it is displaced from the centre, as can be seen in Fig. 13, towards the sides of the contact patch, where the maximum slip velocities take place. In the limit of full slip, the frictional work density is more evenly distributed across the contact patch in the tractive regime than in the braking regime, due to the competing maximum contact stresses of the central part with the maximum slip velocities of the sides of the contact patch in the tractive regime.

It has to be taken into account that the described characteristics for the braking and for the tractive regimes, are for a concave wheel rolling on a convex rail. If a convex wheel –or ball– rolling on a concave rail –or groove– is considered, the different behaviour described here for the two regimes is interchanged. The differing behaviour in the braking and the tractive situations in the conformal rolling contact case considered here, contrasts with what happens in non-conformal rolling contact with elastically similar materials: in the latter case, as it is known, when changing just the sign of the creepages, just the sign of the tangential tractions is changed.

3.3.3. Longitudinal creep-force curve

Going back to Figs. 11 and 12 in Section 3.3.1, it can be seen that the agreement between the results obtained with FEM and with CECT is reasonably good. However, higher discrepancies are observed between the two models in the tangential part of the contact problem than in the normal part. For example, comparing the lateral distributions of W_{fric}, the maximum differences between both models with respect to the maximum values computed for each case with FEM are about 8% in the braking case of Figs. 11 and 6% in the tractive case of Fig. 12. The tangential traction distributions obtained with both models, although being qualitatively quite similar in the contact patch as a whole as seen in Figs. 11 and 12, present non-negligible differences between each other. As an example, in Fig. 14a the distributions of longitudinal tractions p_x along the central longitudinal strip of the contact patch obtained with both models in the tractive case of Fig. 12, are compared.

Additionally, as has been previously mentioned, in order to obtain the same resultant longitudinal contact force F_x, it has been necessary to
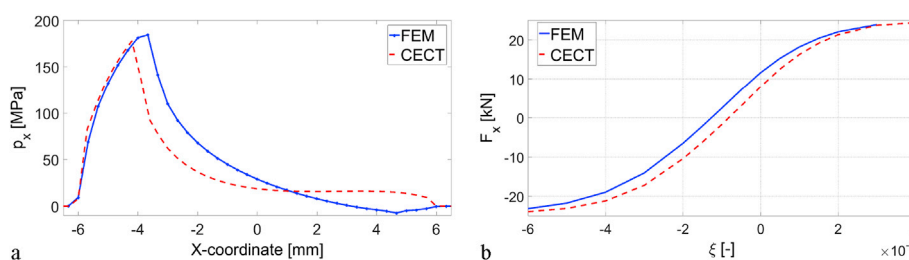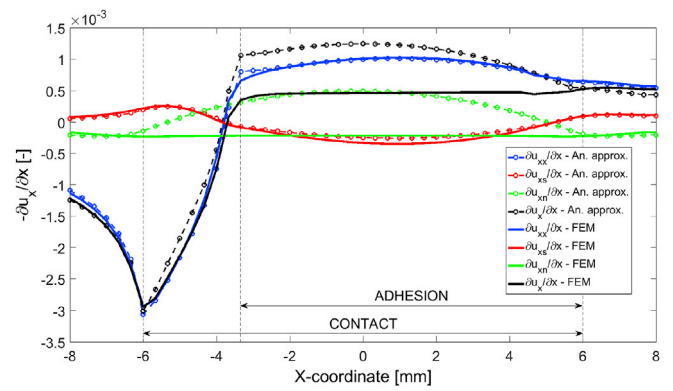

Fig. 15. Gradients of the longitudinal elastic displacement differences with respect to the longitudinal x coordinate with changed sign, $-\partial u_{xi}/\partial x$, along the x direction at $s = 0$, caused by the different tractions p_i in the contact patch in the tractive case of Fig. 12a. Gradients corresponding to the different components of u_x in different colours as follows: u_{xx} in blue, u_{xs} in red, u_{xn} in green and total u_x in black lines. Solid thick lines: results computed with FEM numerical ICs. Dashed thin lines with circle marks: results computed with analytical approximation of ICs for non-planar geometries. (For interpretation of the references to colour in this figure legend, the reader is referred to the web version of this article.)

apply different longitudinal creepages ξ in the FEM models on the one hand, and in the calculations with CECT on the other hand. This can be seen comparing the longitudinal creepage-creep force curves computed with both models shown in Fig. 14b. As seen in the figure, the slopes of the longitudinal creepage-creep force curves computed with FEM and with CECT are similar (the maximum slope of the curve computed with FEM is just about 4% lower than that of the curve computed with CECT), but there is an offset between both curves, and for the same longitudinal creepage, the curve computed with FEM renders higher tractive longitudinal forces than the curve computed with CECT.

In order to understand these discrepancies, the elastic displacements in the longitudinal direction u_x computed with both models are examined in detail. The total longitudinal elastic displacement difference between the two contacting surfaces u_x may be decomposed in the contributions from the tangential longitudinal tractions p_x, the tangential lateral tractions p_s and the normal pressures p_n, as indicated in Eq. (6).

$$u_x = u_{xx} + u_{xs} + u_{xn} = B_{xx} \times p_x + B_{xs} \times p_s + B_{xn} \times p_n \qquad (6)$$

In Eq. (6), u_{xi} is the longitudinal displacement difference caused by the traction in the direction i (with i equal to x, s or n), and B_{xi} is the IC giving the longitudinal elastic displacement difference due to a unitary traction in the direction i. This equation may be written for any pair of points in the contact patch, or for the entire contact patch, putting the whole matrices of ICs $[B_{xi}]$ and the vectors of tractions $\{p_i\}$ and displacement differences $\{u_{xi}\}$ for all the points of the discretization of the contact area in the latter case.

With the purpose of performing this decomposition of the elastic displacement differences $\{u_x\}$ obtained with the FEM models, the matrices of ICs $[B_{xi}]$ of the FEM models have been derived applying

Fig. 14. a) Longitudinal tractions p_x along the contact patch at $s = 0$, in the tractive case of Fig. 12. b) Longitudinal creepage-creep force curve for Case 1, with zero yaw angle and lateral creepage. Blue solid lines: FEM results. Red dashed lines: results computed with CECT. (For interpretation of the references to colour in this figure legend, the reader is referred to the web version of this article.)

unitary tractions at each lateral position of the FE mesh for both the wheel and the rail, and extracting the elastic displacements throughout the contact patch for each load case. To obtain the desired matrices of ICs, these extracted displacements are further processed arranging them in a suitable order and performing the necessary interpolations to map the obtained displacements of the wheel and the rail into a common mesh (the mesh of the potential contact area, similar to that defined in the implementation of the exact contact theory).

In Fig. 15 the gradients with respect to the longitudinal x direction of the longitudinal elastic displacement differences u_{xi} caused by the different tractions p_i acting in the contact patch in the tractive rolling contact situation of Fig. 12a are represented along the centreline of the contact patch (i.e. along the x direction, at $s = 0$). The results corresponding to both the FE model and to CECT are shown in the figure. The gradients of the longitudinal elastic displacement differences with respect to the x direction $\partial u_{xi}/\partial x$, rather than the elastic displacement differences u_{xi}, are shown, because the gradients are the ones which enter directly in the basic kinematic equation of the tangential part of the contact problem, as indicated in Eq. (7).

$$v_{rel} = w_{rel} - \partial u/\partial x + 1/V \, \partial u/\partial t \tag{7}$$

In Eq. (7), v_{rel}, w_{rel} and u are the vectors containing respectively the relative slip velocities, the relative rigid slip velocities and the elastic displacement differences in both principal directions (longitudinal x and lateral s) of the local tangent contact plane at each point, and V is the rolling velocity. The relative slip velocities are defined as the absolute slip velocities divided by the rolling velocity. In steady state rolling contact as are the cases shown in this work, the last, transient term of the right hand side of Eq. (7) vanishes. Additionally, in the adhesion area, $v_{rel} = 0$, and therefore $\partial u/\partial x = w_{rel}$ at each point in the adhesion area in steady state rolling.

In order to observe more clearly the differences between both models, the longitudinal elastic displacement differences for both models shown in Fig. 15 have been computed with the tractions obtained with the FE model. That is, on the one hand, the longitudinal elastic displacement differences corresponding to the FE model are computed with the tractions obtained with the FE model, and with the "real" ICs computed numerically with the FE model. And on the other hand, the longitudinal elastic displacement differences corresponding to CECT are computed with the tractions obtained with the FE model as well, and with the analytical approximation of the ICs for non-planar geometries proposed in Ref. [23], which has been used in CECT in this work. In this way, the displacement differences computed for the FE model are the actual ones corresponding to the tractive rolling contact situation of Fig. 12a, but those computed for CECT do not correspond to any of the rolling contact cases shown here.

As can be seen in Fig. 15, the contributions from the tangential longitudinal and lateral contact stresses p_x and p_s to the longitudinal elastic displacement differences are similar with both sets of ICs. However, there is an appreciable difference in the contribution coming from the normal pressures p_n. So it is concluded that the differences seen in this Section in the results of the tangential part of the contact problem between the FE models and CECT come mainly from the B_{xn} ICs. A sample of the combined B_{xn} ICs of the elastic displacement differences between both contacting bodies computed with the FE models and with the analytical approximation for non-planar geometries are compared in Fig. 16.

First, in Fig. 16a the B_{xn} ICs are plotted together with the B_{xx} ICs, and in Fig. 16b the B_{xn} ICs are plotted alone. It may be striking to see that the B_{xn} ICs can reach such an appreciable effect on the results of the tangential part of the contact problem, in spite that they seem insignificant in comparison with the B_{xx} ICs (in fact they are about two orders of magnitude lower), which produce the dominant u_{xx} contribution to the total longitudinal elastic displacement difference u_x in this case. But it has to be taken into account that in the considered cases the normal pressures in the contact patch are considerably higher than the tangential stresses,

and that the B_{xn} ICs reverse their sign with the longitudinal distance x_{rel} from the centre of the loaded element, while the B_{xx} ICs don't. It has to be mentioned as well that the u_{xx} contribution of the longitudinal displacement differences has a high constant component, which does not contribute to its gradient in the longitudinal direction.

As can be seen in Fig. 16b, there is a clear discrepancy between the "real" B_{xn} ICs obtained from the FE model, and the B_{xn} ICs computed with the analytical approximation for non-planar geometries. This can be explained looking at the individual ICs of the displacements of each of the contacting bodies shown in Fig. 17: the B_{xn} ICs of the concave wheel are lower than the corresponding half-space ICs, while the B_{xn} ICs of the convex rail are higher. This is due to the higher stiffness in the longitudinal direction of the wheel than that of the rail. This effect, which depends not only on the contact angle variation in the contact patch but also on the overall geometry of the cross sections of the solids in contact, is not taken into account with the analytical approximation of the ICs for non-planar geometries used in this work. Something similar happens with the B_{xx} and the B_{xs} ICs. However, in the combined ICs giving the displacement differences between both contacting bodies, the differences in the ICs of each of the contacting bodies cancel each other in the case of the B_{xx} and the B_{xs} ICs, while they sum to each other in the case of the B_{xn} ICs.

The consequences of the difference in the longitudinal stiffness of both contacting bodies on the contributions to the longitudinal elastic displacement differences caused by the normal pressures can be easily understood considering for simplification the effect of the normal pressures in planar geometries. As it is known, in planar geometries the normal compressive loads tend to move the surrounding surface points towards where the load is applied. If the wheel is stiffer than the rail, in the front or leading part of the contact patch the points of the rail will have a backwards displacement with respect to the points of the wheel as a result of the normal pressures, and conversely, in the back or trailing part of the contact patch the points of the rail will have a forward displacement with respect to the points of the wheel. So as the points of the wheel and the rail traverse the contact patch from the leading to the trailing edge, the points of the wheel have a relative backwards longitudinal displacement with respect to the points of the rail. The net effect is similar to having an extra tractive creepage applied. In the case of non-planar geometries, the picture is not so clear because the B_{xn} ICs reverse their sign not only at $x_{rel} = 0$, as can be seen in the curve corresponding to the FEM results of Fig. 16b. Nevertheless, in the considered case the effect is in the same sense as anticipated with the reasoning for planar geometries in the majority of the contact patch, and only in the most lateral parts of the contact area this effect is reversed.

Lastly, it is noted again that a concave wheel rolling on a convex rail has been considered. In the case of having a convex wheel rolling on a concave rail, the rail would be stiffer than the wheel in the x direction, and the offset between the longitudinal creepage-creep force curves calculated with CECT (with the analytical approximation of the ICs for non-planar geometries used in this work) on the one hand and with FEM on the other hand would happen in the opposite sense.

4. Conclusions

A detailed investigation of 3D frictional conformal contact has been carried out, in situations with different conformity levels, up to total contact angle variations in the contact patch $\Delta\delta$ of about $100°$. The study has been focused in steel-on-steel contact, which is present in some important industrial applications like rolling bearings and the wheel-rail contact in railway vehicles. Models with varying degrees of complexity have been used in the study, from the Hertzian model, to the rigorous exact rolling contact theory properly extended for conformal contact (named here as CECT), and to comprehensive FE models.

As was illustrated in Ref. [23], when using the exact contact theory to study conformal contact problems, it is essential to use realistic normal undeformed distances in the normal part of the contact problem and rigid slip velocities in the tangential part of the contact problem, which may
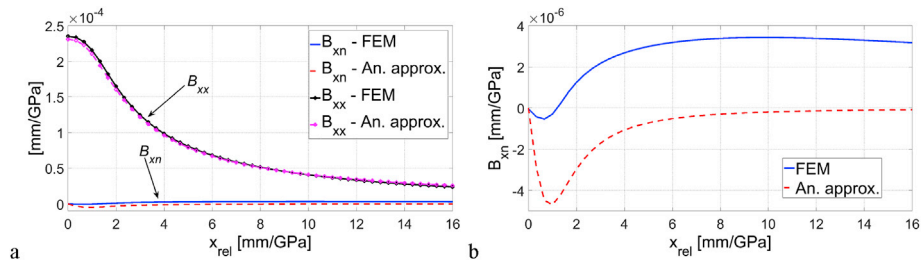
Fig. 16. Combined B_{xn} and B_{xx} ICs of the elastic displacement differences between both contacting bodies along the longitudinal direction at $s = 0$, as a function of the longitudinal distance x_{rel} from the centre of the loaded element. The loaded element has a longitudinal dimension dx of 0.33 mm, a lateral dimension ds of 0.32 mm, its centre is located at $s = 1.26$ mm, and it is loaded with an uniform load. a) B_{xn} and B_{xx}. A value of 1.128×10^{-5} mm/GPa has been substracted from the B_{xx} ICs computed with FEM in order to account for the global displacements present in the FE models. b) B_{xn}. Blue and black solid lines: FEM results. Red and magenta dashed lines: analytical approximation for non-planar geometries. B_{xn} anti-symmetric, and B_{xx} symmetric with respect to $x_{rel} = 0$. (For interpretation of the references to colour in this figure legend, the reader is referred to the web version of this article.)

deviate considerably from those calculated in the usual "non-conformal" way. Nevertheless, in some situations even a simple Hertzian calculation can provide quite accurate figures for the most representative magnitudes of the normal part of the contact problem up to considerable levels of conformity. As an example, two simple geometries were studied, with constant curvatures in the contact patch, zero mean contact angle and yaw angle, and with different ratios of the longitudinal to the lateral dimensions of the resulting contact patches. It is found that the effects of conformity begin to be appreciable in the tangential part of the contact problem first, but as $\Delta\delta$ increases they have to be taken into account in the normal part of the contact problem as well. Other conclusions of the study are listed below:

- A Hertzian calculation can provide good results in the normal part of the contact problem up to considerable degrees of conformity, with a $\Delta\delta$ of at least 40°.
- A correction is proposed for the combined lateral B curvature of the contact, which considerably improves the results provided by the Hertzian theory in conformal contact, especially in cases with low length to width ratio of the contact patch.
- The use of the half-space influence coefficients for the normal part of the contact problem in the exact contact theory is a good approximation up to moderate $\Delta\delta$s in the contact patch. However, with higher $\Delta\delta$s, it becomes necessary to use more accurate ICs to obtain precise results. In order to avoid the calculation of the ICs for each particular geometry, an approximation of the ICs of non-planar geometries may be made, based on the ICs of the half-space, which are readily

available. This approximation has been seen to substantially improve the results obtained with the direct use of the half-space ICs.
- The use of accurate ICs for the exact contact theory is more important with contact patches with high length to width ratios, due to the higher cross influence between the different longitudinal strips of the contact patch.
- In cases with constant curvatures in the contact patch, the contact patches deviate from the Hertzian elliptic shape as $\Delta\delta$ increases, tending to become more square-shaped.
- The qualitative behaviour of the tangential stresses which are present in frictional static conformal contact even in the absence of net longitudinal or lateral forces, does not seem to be significantly affected by the ratio of the longitudinal to the lateral dimensions of the contact patch. These tangential stresses increase in magnitude with $\Delta\delta$, and should be taken into account for proper damage evaluation when significant friction is present in the contact interface.
- In contrast to non-conformal rolling contact with elastically similar materials, in conformal rolling contact different characteristics are observed in the tangential part of the contact problem depending on the sign of the creepages. Considering the rolling of a concave wheel on a convex rail, in situations with zero mean contact angles and lateral creepages, the adhesion area in the contact patch tends to be more acute shaped, and more extended in the longitudinal direction, in tractive rolling than in braking rolling. On the other hand, the frictional work density tends to be more evenly distributed across the width of the contact area in tractive rolling, while it is more concentrated in the central region of the contact patch in braking rolling.
- As a result of the non-planar geometry of the contacting bodies, there is a difference between the longitudinal stiffness of both contacting bodies, in spite of having elastically identical materials. This difference has an effect similar to having an additional longitudinal creepage (similar to what happens in non-conformal rolling when the materials of the wheel and the rail are dissimilar), and gives rise to an offset in the longitudinal creepage-creep force curve, although the slope of the curve is not altered significantly.
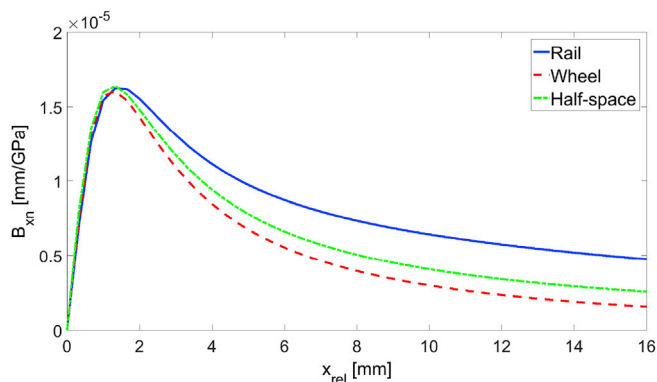
In its current implementation, the CECT model is particularized to a straight rail geometry in the rolling direction, but the necessary changes to account for a curved geometry in the rolling direction of both contacting bodies would be relatively straightforward. An interesting topic for further research could be to use the CECT model in a rolling bearings application, after performing these modifications.

In the studied cases the computational costs have been found to be roughly three orders of magnitude higher with the FE models than with CECT. This figure is to be considered only as orientative, as the run times vary considerably from case to case, and may also depend on a number of circumstances other than the physical models themselves, such as convergence tolerance settings or the particular algorithmic implementation of the models. The exact contact theory, while having much

Fig. 17. B_{xn} ICs of the displacements of each of the contacting bodies computed with FEM, and of the half-space, along the longitudinal direction at $s = 0$, as a function of the longitudinal distance x_{rel} from the centre of the loaded element. The loaded element has a longitudinal dimension dx of 0.33 mm, a lateral dimension ds of 0.32 mm, its centre is located at $s = 1.26$ mm, and it is loaded with an uniform load. Blue solid line: rail. Red dashed line: wheel. Green dash-dotted line: half-space. Results anti-symmetric with respect to $x_{rel} = 0$. (For interpretation of the references to colour in this figure legend, the reader is referred to the web version of this article.)

lower computational costs than the FE models, has been proved to produce good results with high levels of conformity, being capable to capture the particular characteristics of conformal contact both in the normal and in the tangential parts of the contact problem.

Acknowledgements

Appendix A. Supplementary data

Supplementary data related to this article can be found at https://doi.org/10.1016/j.triboint.2017.10.022.

References

[1] Persson A. On the stress distribution of cylindrical elastic bodies in contact. Ph.D. dissertation. Goteborg, Sweden: Chalmers, Tekniska; 1964.

[2] Ciavarella M, Decuzzi P. The state of stress induced by the plane frictionless cylindrical contact. I. The case of elastic similarity. Int J Solids Struct 2001;38: 4507–23.

[3] Ciavarella M, Decuzzi P. The state of stress induced by the plane frictionless cylindrical contact. II. The general case (elastic dissimilarity). Int J Solids Struct 2001;38:4525–33.

[4] Hou JP, Hills DA. Contact between a pin and a plate with a hole under interference-fit and clearance-fit conditions. Proc Inst Mech Eng Part C J Mech Eng Sci 2001;215: 629–39.

[5] Sundaram N, Farris TN. The generalized advancing conformal contact problem with friction, pin loads and remote loading – case of rigid pin. Int J Solids Struct 2010;47: 801–15.

[6] Sundaram N, Farris TN. Mechanics of advancing pin-loaded contacts with friction. J Mech Phys Solids 2010;58:1819–33.

[7] Liu S, Chen WW. Two-dimensional numerical analyses of double conforming contacts with effect of curvature. Int J Solids Struct 2012;49:1365–74.

[8] Liu S. Numerical simulation of double conformal contacts involving both interference and clearance. Tribol Trans 2013;56(5):867–78. https://doi.org/10.1080/10402004.2013.806686.

[9] Ciavarella M, Baldini A, Barber JR, Strozzi A. Reduced dependence on loading parameters in almost conforming contacts. Int J Mech Sci 2006;48:917–25.

[10] Woodward W, Paul B. Contact stresses for closely conforming bodies–application to cylinders and spheres. Department of Mechanical Engineering and Applied Mechanics, University of Pennsylvania; 1976 (Report no DOT-TST-77–48).

[11] Paul B, Hashemi J. Numerical determination of contact pressures between closely conforming wheels and rails. Department of Mechanical Engineering and Applied Mechanics, University of Pennsylvania; 1979 (Report no FRA/ORD-79–41).

[12] Piotrowski J, Kik W. The influence of spin on creep forces for non-flat contact area. Veh Syst Dyn 1999 1999;31(suppl.):158–77.

[13] Kalker JJ. Three-dimensional elastic bodies in rolling contact. The Netherlands: Kluwer Academic Publishers; 1990.

[14] Kalker JJ. Rolling contact phenomena - linear elasticity. In: Jacobson B, Kalker JJ, editors. Rolling contact phenomena, CISM courses and lectures. Wien, New York: Springer; 2001. p. 1–84. No. 411, Chapter 1.

[15] Johnson KL. Contact mechanics. Cambridge: Cambridge University Press; 1985.

[16] Ayasse JB, Chollet H. Determination of the wheel rail contact patch in semi-Hertzian conditions. Veh Syst Dyn 2005;43:161–72. https://doi.org/10.1080/00423110412331327193.

[17] Quost X, Sebes M, Eddhahak A, Ayasse J, Chollet H, Gautier P, et al. Assessment of a semi-Hertzian method for determination of wheel-rail contact patch. Veh Syst Dyn 2006;44:789–814. https://doi.org/10.1080/00423110600677948.

[18] Li Z. Wheel-rail rolling contact and its application to wear simulation. Ph.D. dissertation,. The Netherlands: Technische Universiteit Delft; 2002.

[19] Burgelman N, Li Z, Dollevoet R. A new rolling contact method applied to conformal contact and the train–turnout interaction. Wear 2014;321:94–105. https://doi.org/10.1016/j.wear.2014.10.008.

[20] Vollebregt E, Segal G. Solving conformal wheel–rail rolling contact problems. Veh Syst Dyn 2014;52(suppl.):455–68.

[21] Vollebregt E. User guide for CONTACT. Delft: VORtechBV; 2013., version 13.1. www.kalkersoftware.org.

[22] Blanco-Lorenzo J, Santamaria J, Vadillo EG, Correa N. Finite element study of wheel-rail conformal rolling contact. Graz, 17–21 August. In: Jost Bernasch, Martin Rosenberger, editors. Dynamics of vehicles on roads and tracks; 2015.

[23] Blanco-Lorenzo J, Santamaria J, Vadillo EG, Correa N. On the influence of conformity on wheel-rail rolling contact mechanics. Tribol Int 2016;103:647–67.

[24] Toumi M, Chollet H, Yin H. Finite element analysis of the frictional wheel-rail rolling contact using explicit and implicit methods. Wear 2016;366–367:157–66.

[25] Vollebregt EAH. 100-fold speed-up of the normal contact problem and other recent developments in "CONTACT". 9th International Conference on Contact Mechanics and Wear of Rail/Wheel Systems (CM2012), Chengdu, China, August 27-30, 2012.

[26] Zhao J, Vollebregt EAH, Oosterlee CW. A fast nonlinear conjugate gradient based method for 3D concentrated frictional contact problems. J Comput Phys 2015;288: 86–100.

[27] Sichani MS, Enblom R, Berg M. A novel method to model wheel-rail normal contact in vehicle dynamics simulation. Veh Syst Dyn 2014;52(12):1752–64.

[28] Popov VL. Contact mechanics and friction. Physical principles and applications. Berlin: Springer-Verlag; 2010.